Numerical modeling of the secondary droplet break-up in spray flows

C. Sula[1*], M. V. Papalexandris[1], H. Grosshans [2]
[1]Institute of Mechanics, Materials and Civil Engineering,
Université catholique de Louvain, 1348 Louvain-la-Neuve, Belgium
[2]Physikalisch-Technische Bundesanstalt (PTB), Bundesallee 100, 38116 Braunschweig, Germany

Abstract

The break-up and evaporation of liquid jets is crucial to the efficiency of the combustion process in direct injection engines. Despite its importance, no final consensus concerning the mathematical framework to compute sprays has been reached yet. In the current study we perform simulations of n-dodecane jets with three different models and make comparisons of their predictive capacities. These are the Taylor Analogy Breakup, Reitz-Diwakar and Pilch Erdman models. The values of the model parameters that we use for our simulations are those typically used in the studies of fuel injection in diesel engines. The numerical setup is based on the Engine Combustion Network "Spray A" operating conditions. Due to the high Reynolds numbers of the flow, the motion of the surrounding air is treated numerically via Large Eddy Simulations (LES), whereas the motion of the droplets is tracked in the Lagrangian framework, assuming two-way coupling between the two phases.

1. Introduction

Diesel engines continue to be an important technology for energy transformation in many industries. Both economical and environmental factors have played a role in encouraging the automotive, transportation and energy generation industries to develop new strategies to improve performance in diesel engines. One of the main issues for diesel engines is that on-road emissions are higher than those seen in test cycles. For the last decade, technological advances and development of new optical techniques have made possible the investigation of quantitative parameters of the spray in diesel engines prior to combustion [1].

Recent theoretical and experimental research shows that injection spray characteristics have a significant influence on combustion performance, including the impact on dynamics and composition of the emission gases. Therefore, a fuller understanding of the physics of spray formation, will likely result in the development of new technologies for fuel injection. This will improve the combustion process as a whole and thus reduce emissions.

Spray formation is a complex process and includes several different phenomena occurring both rapidly and simultaneously, such as high-velocity jet flow, liquid droplet break-up, atomization, and evaporation of the liquid spray in a turbulent domain. The small spatial and temporal scales characterizing these phenomena makes spray evolution a complicated problem to study both experimentally and numerically.

Computational Fluid Dynamics (CFD) simulations of engine in-cylinder processes is of the utmost importance in the combustion design process, but care has to be taken as there are still several unresolved issues in spray combustion modeling. In particular, the correct modeling of the spray-turbulence interaction will influence greatly the prediction of fuel liquid and vapor penetration and mixture formation. These three parameters are important for the quantification of the quality of the reacting mixture.

The liquid penetration characterizes the spray from a macroscopic point, in that it describes the evaporation capacity of the fuel. The air-fuel vapor mixing process is strongly influenced by the fuel vapor penetration, which essentially depends on the instantaneous momentum of the spray in the nozzle.

In the present study we compare numerical simulations against experimental results for both liquid and vapor penetration, in order to quantify differences between three popular secondary-break-up models. These are the Taylor Analogy Breakup, Reitz-Diwakar and Pilch Erdman models. The values of the model parameters that we use for our simulations are those typically used in the studies of fuel injection in diesel engines. The numerical setup is based on the Engine Combustion Network "Spray A" operating conditions.

The article is structured as follows: Section 2 provides the governing equations for the flow of interest, Section 3 provides a brief description of the the secondary break-up models, in Section 4 the computational set-up and simulation results are discussed finally in Section 5 we summarize the most important outcomes of the research.

2. Governing Equations

In our study we have carried out Large Eddy Simulations (LES), we therefore consider the spatially-filtered Navier-Stokes equations. More specifically, we employ the density-weighted operator of Favre [2]. Applied to a generic quantity ϕ, the corresponding Favre-filtered $\widetilde{\phi}$ is

*Corresponding author: constantin.sula@uclouvain.be
Proceedings of the European Combustion Meeting 2019

defined by $\widetilde{\phi} = \overline{\rho\phi}/\overline{\rho}$, where $\overline{\rho}$ and $\overline{\rho\phi}$ are spatially-filtered quantities. Upon Favre-filtering the governing equations describing the balance of mass, momentum, energy and species, read:

$$\begin{aligned}
\frac{\partial\overline{\rho}}{\partial t} + \nabla\cdot(\overline{\rho}\widetilde{\boldsymbol{u}}) =& \overline{\dot{m}_{\rm s}},\\
\frac{\partial\overline{\rho}\widetilde{\boldsymbol{u}}}{\partial t} + \nabla\cdot(\overline{\rho}\widetilde{\boldsymbol{u}}\widetilde{\boldsymbol{u}}) =& -\nabla\overline{p} + \nabla\cdot((\overline{\mu}+\mu_{\rm t})\widetilde{\boldsymbol{\sigma}})\\
&+ \overline{\dot{F}_s},\\
\frac{\partial(\overline{\rho}\widetilde{E})}{\partial t} + \nabla\cdot(\overline{\rho}\widetilde{E}\widetilde{\boldsymbol{u}}) =& -\nabla\cdot(\overline{p}\widetilde{\boldsymbol{u}}) + \nabla\cdot(\widetilde{\boldsymbol{\sigma}}\cdot\widetilde{\boldsymbol{u}})\\
&+ \nabla\cdot((\overline{\kappa}+\kappa_{\rm t})\nabla\widetilde{T}) + \overline{\dot{Q}_{\rm s}},\\
\frac{\partial\overline{\rho}\widetilde{Y_i}}{\partial t} + \nabla\cdot(\overline{\rho}\widetilde{\boldsymbol{u}}\widetilde{Y_i}) =& \nabla\cdot(\overline{\rho}(\overline{D_i}+D_{i\rm t})\nabla\widetilde{Y_i})\\
&+ \overline{\dot{Y}_{i,\rm s}}
\end{aligned} \tag{1}$$

Following standard notation, $\overline{\rho}$, $\overline{p}$, $\widetilde{E}$ and $\widetilde{\boldsymbol{u}} = (\widetilde{u}, \widetilde{v}, \widetilde{w})$ denote, respectively the filtered fluid density, pressure, total energy and velocity vector. $\widetilde{Y}_i$ represents the species mass fraction, where $i = \mathrm{N_2}$, $\mathrm{CO_2}$, $\mathrm{H_2O}$ and fuel vapor. The viscous stress tensor is given by $\widetilde{\sigma}_{ij} = 2\overline{\mu}\widetilde{S}^*_{ij}$, where S^*_{ij} is the traceless strain-rate tensor. Further, μ, κ and D_i represent the fluid viscosity, thermal conductivity and spicies diffusivities, respectivelly. Herein, for each species we consider binary diffusion with respect to the dominant constituent $\mathrm{N_2}$.

With regard to subgrid-scale modeling, the eddy viscosity $\mu_{\rm t}$ is computed via the dynamic k-equation LES model [3], [4], whereas constant values are assumed for the eddy conductivity $\kappa_{\rm t}$ and eddy diffusivities $D_{i\rm t}$.

In the governing system (1) the source terms $\overline{\dot{m}_{\rm s}}$, $\overline{\dot{F}_{\rm s}}$, $\overline{\dot{Q}_{\rm s}}$ and $\overline{\dot{Y}_{i,\rm s}}$ describe the interactions between the continuous gaseous phase and the dispersed liquid phase. More specifically, $\overline{\dot{m}_{\rm s}}$ accounts for the phase change, i.e. the evaporation of the liquid fuel. The source term $\overline{\dot{F}_{\rm s}}$ accounts for the momentum transfer between the droplets and the carrier fluid. Its integral over a control volume is equal to the opposite of the sum of the aerodynamic drag forces acting on the droplets present. Further, the source term $\overline{\dot{Q}_{\rm s}}$ represents the energy transfer between the droplets and the carrier fluid. Its integral over a control volume is equal to the opposite of the sum of the energy that a single droplet exchanges with the fluid. For any given droplet, this energy exchange consists of 3 contributions: heat transfer, latent heat of evaporation and the work of the aerodynamic drag. Due to the fact that no chemical reaction occurs between the species, the overall mass of $\mathrm{N_2}$, $\mathrm{CO_2}$ and $\mathrm{H_2O}$ remains constant. Therefore, in the equations for the species concentrations, only $\overline{\dot{Y}}_{\rm fuels,s}$ is non-zero, and the following relation holds $\overline{\rho}\overline{\dot{Y}}_{\rm fuel,s} = \overline{\dot{m}}_{\rm s}$. The system of equation is closed by the thermal equation of state $\overline{p} = \overline{\rho}\widetilde{RT}$.

The motion of the droplets is computed numerically by combining Lagrangian Particle Tracking (LPT) and the stochastic parcel method. According to this procedure, the droplets are grouped into parcels and the characteristics of the droplets within a parcel (number, diameter, velocity, temperature) are determined by a probability distribution function f e.g for particle diameter Rosin-Rammler distribution is considered [5]. For numerical purposes, each parcel is treated as a Lagrangian point particle and is tracked individually. The particle dynamics is described by Newton's equation of motion, with the aerodynamic drag being the only force acting on a liquid particle. In this manner, we have the following equation of motion:

$$\frac{d\boldsymbol{u}_{\rm d}}{dt} = -\frac{3\rho_{\rm g}}{4\rho_{\rm l}d_{\rm d}}C_{\rm D}|\boldsymbol{u}_{\rm rel}|\boldsymbol{u}_{\rm rel}. \tag{2}$$

where $\boldsymbol{u}_{\rm rel}$ denotes the relative velocity between the droplet and the surrounding gas and $d_{\rm d}$ is the particle diameter. Also, in the above expression $C_{\rm D}$ is the drag coefficient and depends on the Reynolds number of the particle. In the present study, $C_{\rm D}$ is computed via correlations provided in [6] for the standard drag curve for a smooth sphere. The contribution of the other forces acting on the the droplet surface, such as the virtual mass, Faxen, Basset term, Magnus and Saffman forces, are considered negligibly small. Accordingly, these forces are neglected, which is a common practice in spray simulation [7], [8].

Finally, for the spray evaporation we employ the model of Amsden et al. [9], which assumes that the droplets are spheres with uniform properties in their interior [9].

3. Secondary Break-up Models

In the problem of interest, the operating conditions are such that both the primary break-up and the atomization occur very close to the nozzle exit. For this reason they are not modeled in the present study. Instead, we assume that we have an already atomized spray. We also assume that collisions between droplets occur very rarely and, therefore, are not taken into account either. Instead, our study focuses on the simulation of the secondary break-up. To this end, three different models for secondary break-up are tested, namely, the Taylor Analogy Break-up (TAB) [10], the Reitz-Diwakar (RD) [11] and the Pilch-Erdman (PE) [12] models. In what follows these models are briefly reviewed.

3.1 Taylor Analogy Break-up

The TAB model has been developed by O'Rourke and Amsden [10]. It is based upon Taylor's analogy between an oscillating and distorting droplet and a spring mass system. The restoring force of the spring corresponds to the surface tension, while the external force on the mass is equivalent to the aerodynamic force. Finally the damping force represents the liquid viscosity effects. The model

keeps track only of the fundamental mode, corresponding to the lowest order harmonic whose axis is aligned with the relative velocity vector between droplet and gas. This mode is dominant for small Weber numbers, while for large Weber numbers other modes are contributing significantly to droplet break-up, where the Weber number We is the ratio between inertial forces to surface tension forces, $We = (\rho_{\mathrm{g}} \boldsymbol{u}_{\mathrm{rel}}^2 d_{\mathrm{d}})/\sigma$. The equation governing a damped, forced oscillator is

$$m\frac{d^2x}{dt^2} = -d\frac{dx}{dt} - kx + F, \tag{3}$$

where x is the displacement of the droplet equator from its spherical (undisturbed) position, F are the external forces (corresponding to aerodynamic drag), k is the spring's constant (corresponding to surface tension) and d the damping parameter (corresponding to viscous forces). In accordance with the Taylor analogy, the physical dependencies of the coefficients in the equation are:

$$\frac{F}{m} = C_f\frac{\rho_{\mathrm{g}}u^2}{\rho_{\mathrm{l}}r}, \quad \frac{k}{m} = C_k\frac{\sigma}{\rho_{\mathrm{l}}r^3}, \quad \frac{d}{m} = C_d\frac{\mu_{\mathrm{l}}}{\rho_{\mathrm{l}}r^2}, \tag{4}$$

where C_f, C_k and C_d are dimensionless coefficients, σ is the gas-liquid surface tension and μ_l is the liquid viscosity. In addition, the dimensionless constant C_b is a scaling parameter in the non-dimensionalization of x by defining $y = x/(C_b r)$. By substituting these expressions the equation of oscillator (4) can be written as:

$$y'' = \frac{C_f}{C_b}\frac{\rho_g}{\rho_l}\frac{u^2}{r^2} - \frac{C_k}{\rho_l}\frac{\sigma}{r^3}y - \frac{C_d}{\rho_l}\frac{\mu_l}{r^2}y' \tag{5}$$

with the break-up occurring if and only if $y > 1$. The constants C_f, C_k, C_d and C_b are from experimental and theoretical results [13], and have the following values : $C_f = 1/3$, $C_k = 8$, $C_d = 5$, and $C_b = 1/2$.

3.2 Reitz-Diwakar Model

The RD model is based on the correlations given by Nicholls [14]. According to it two break-up regimes are identified with respect of the Weber number. Bag break-up occurs when $We > We_{\mathrm{cr}}$ and stripping break-up when $We > C_{s1}\sqrt{Re}$. The decrease of the radius of the unstable droplet follows the relation:

$$\frac{dr_{\mathrm{p}}}{dt} = \frac{-(r_{\mathrm{d}} - r_{\mathrm{st}})}{t_{\mathrm{br}}}, \tag{6}$$

where r_{d} is the droplet radius prior to break-up, r_{st} is the new radius for the stable droplet and t_{br} is the characteristic break-up time. Once the droplet radius reduces to r_{st}, the droplet is considered to be stable and does not disintegrate further. The number of droplets in each parcel after the break-up is determined from the mass conservation within the parcel. The characteristic break-up time and the stable radius for each break-up regime are calculated as follows:

Bag break-up:

$$t_{\mathrm{br}} = C_1\sqrt{\frac{\rho_{\mathrm{l}}r_{\mathrm{d}}^3}{2\sigma}}, \qquad r_{\mathrm{stab}} = \frac{6\sigma}{\rho_{\mathrm{g}}u_{\mathrm{rel}}^2}. \tag{7}$$

Stripping break-up:

$$t_{\mathrm{br}} = C_2\frac{r}{u_{\mathrm{rel}}}\sqrt{\frac{\rho_{\mathrm{l}}}{\rho_{\mathrm{g}}}}, \qquad r_{\mathrm{stab}} = \frac{\sigma^2}{2\rho_{\mathrm{g}}^2u_{\mathrm{rel}}^3\nu}. \tag{8}$$

The values of the constants are set to: $C_1 = \pi$, $C_2 = 20$, $C_{s1} = 0.5$. Also, the critical Weber number is set to $We_{\mathrm{cr}} = 6$.

3.3 Pilch-Erdman Model

According to this model, the droplet deformation and break-up times are calculated from the experimental findings of [12] and [15]. As in the RD model, the break-up can occur if the Weber number is larger then the critical Weber number, We_{cr}, below which droplet break-up does not occur. Therefore, the the droplet break-up process is categorized into different regimes depending on the droplet Weber number. The characteristic dimensionless time of the droplet break-up due to Rayleigh-Taylor and Kelvin-Helmholtz instabilities is given by:

$$T = t\frac{u_{\mathrm{rel}}}{d}\sqrt{\frac{\rho_{\mathrm{g}}}{\rho_{\mathrm{l}}}}. \tag{9}$$

The total break-up time T is defined as the time when the droplet and its fragments no longer undergo further break-up. The following correlation for total break-up time are provided:

$$\begin{aligned}
T =& 6(We - We_{\mathrm{cr}})^{-0.25}, && We_{\mathrm{cr}} \leq We \leq 18,\\
T =& 2.45(We - 12)^{0.25}, && 18 \leq We \leq 45,\\
T =& 14.1(We - 12)^{0.25}, && 45 \leq We \leq 351,\\
T =& 0.766(We - 12)^{0.25}, && 351 \leq We \leq 2670,\\
T =& 55, && 2670 \leq We.
\end{aligned}$$

When the Ohnesorge number $Oh = \sqrt{We}/Re$ is small, i.e. $Oh < 0.1$, then $We_{\mathrm{cr}} \simeq 12$, which is the value used in our study.

4. Numerical Setup

Numerical simulations have been carried out under a set of conditions named Spray A by the Engine Combustion Network (ECN). Experimental results of Spray A have been obtained from Sandia National Laboratories through the ECN [16], and have been chosen as a reference for comparison in this study. Liquid n-dodecane is injected

Spray details	
Fuel	n-dodecane ($C_{12}H_{26}$)
Fuel temperature [K]	363
Nozzle diameter [μm]	90
Injection pressure [MPa]	150
Injection duration [ms]	1.5
Injected fuel mass [mg]	3.5

Ambient conditions	
Temperature [K]	900
Density [kg/m^3]	22.8
Pressure [MPa]	6

Table 1: Case details.

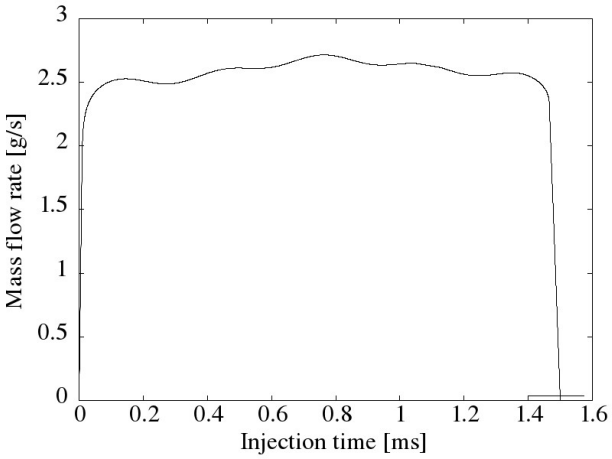

Figure 1: Fuel mass flow rate profile.

through a 90 μm diameter nozzle into a gas of temperature 900 K and initial gas density of 22.8 kg/m^3.

Initially, the molar composition of the gas is: $N_2 = 89.71\%$, $CO_2 = 6.52\%$ and $H_2O = 3.77\%$. Herein we examine a flow without combustion, so the concentration of O_2 is set to zero. The various thermophysical properties change significantly within the temperature range considered in our study. Their values are computed via the well known 9th-order polynomial correlations developed by NASA [17]. The initial thermodynamic conditions are summarized in Table 1. Also, the injected mass flow rate profile is shown in Figure 1.

The droplet distribution resulting from the primary break-up of the liquid jet is directly imposed at the mozzle outlet. The initial droplet diameters are determined by a Rosin-Rammler distribution with parameters that lead to an initial Sauter mean diameter of $\approx 15\mu$m. The amount of injected parcels over the duration of the simulation is 750 000.

The computational domain is a cuboid with a crossflow section equal to 20 mm $\times$ 20 mm and streamwise length equal to 80 mm. In order to improve the computational

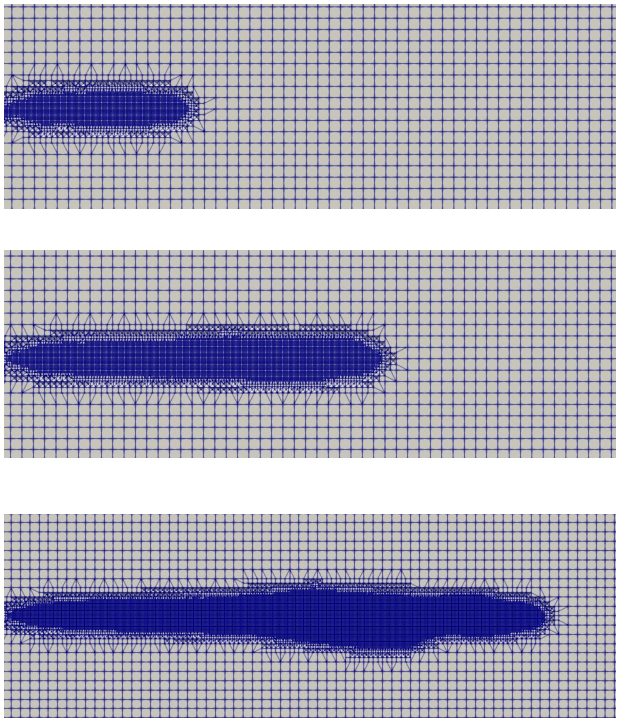

Figure 2: Resulting mesh refinement using vaporized fuel fraction at 0.05 ms, 0.1 ms and 0.2 ms

accuracy, an adaptive mesh refinement (AMR) with 3 levels of refinement is implemented based on the fuel vapor fraction. This results in a mesh composed of 2.1 million cells. The largest cell size is 0.4 mm while the smallest is 0.05 mm, close to the injection position, Figure 2 shows the dynamic evolution of the mesh.

The simulations have been performed with compressible LES solver sprayFoam, of the open-source CFD software OpenFOAM [18]. Under the given condition it takes a little less then 2 seconds for the injected fuel to evaporate completely. For this reason the final time of the simulations is set at t_F =2 s.

5. Numerical Results and Discussion

The principal global quantities against which we will compare our simulations are liquid penetration and vapor fuel penetration. The liquid penetration is defined as the maximum distance from the nozzle outlet to the farthest axial position for 0.1% liquid volume fraction, averaged over a cylindrical volume of 1 mm diameter and 1 mm axial length [16].

Figure 3 plots the liquid penetration length against time for all three simulations together with the experimental data of Sandia Spray A. From Figure 3 three distinct phases of the transient can be identified. In the first phase, from the start of the injection until 0.07 ms there is a rapid increase in fuel penetration length up to 0.7-0.8 mm.

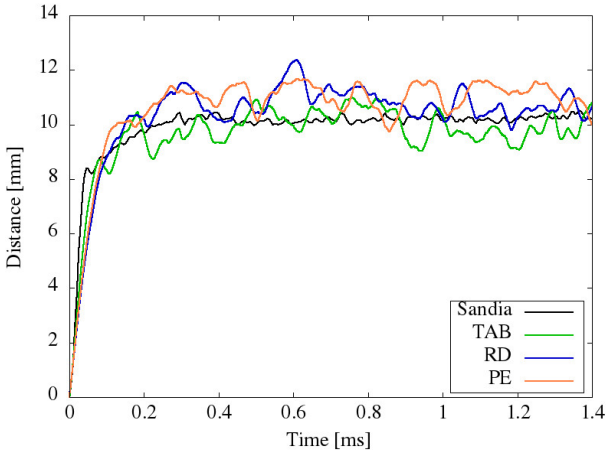

Figure 3: Liquid penetration length.

In this phase the liquid penetration is governed by the initial velocity and direction of the parcels. At this early time, droplet evaporation rate is small and does not affect the liquid penetration length. This can be corroborated by the small values of the fuel vapor mass fraction in the region close to the nozzle as shown in Figure 4.

In the second phase, from approximately 0.1 ms until 0.25 ms the increase in liquid length penetration begins to slow down until finally, in the third phase, the liquid penetration length remain nearly constant. This signal the completion of the evaporation of the droplets. This final phase represents a statistically stationary spray, and lasts until the end of the injection. The role of evaporation is dominant in the final phase due to the decreasing droplet diameter. According to Figure 4, the fuel mass fraction increases with distance from the injection position, which further suggests that evaporation is dominant downstream. What is more, the flow become turbulent, enhancing the mixing process, this can be observed by comparing the temperature field Figure 5 with fuel mass fraction field Figure 4.

According to our simulations, the RD and PE models over-predicted the liquid penetration length, while the first phase of the liquid length penetration is not well captured. By contrast the TAB model, the fuel penetration at the beginning is better captured, while in the final stationary spray phase, the liquid length penetration is slightly under-predicted. This is because the TAB model accounts for the velocity-dependent harmonic oscillations, which tend to accelerate the disintegration of the droplets and consequently, faster evaporation. In all three simulations fluctuations are observed in the liquid penetration length in the stationary spray phase and a higher compared to the experimental results. This is likely due to the small number of parcels that are injected during the whole simulation.

The vapor penetration length is defined as the distance from the nozzle to the tip of the vapor fuel plume, at which the mass fraction of the vapor fuel is 0.1%. Figure 6 shows the vapor penetration length evolution with time for all

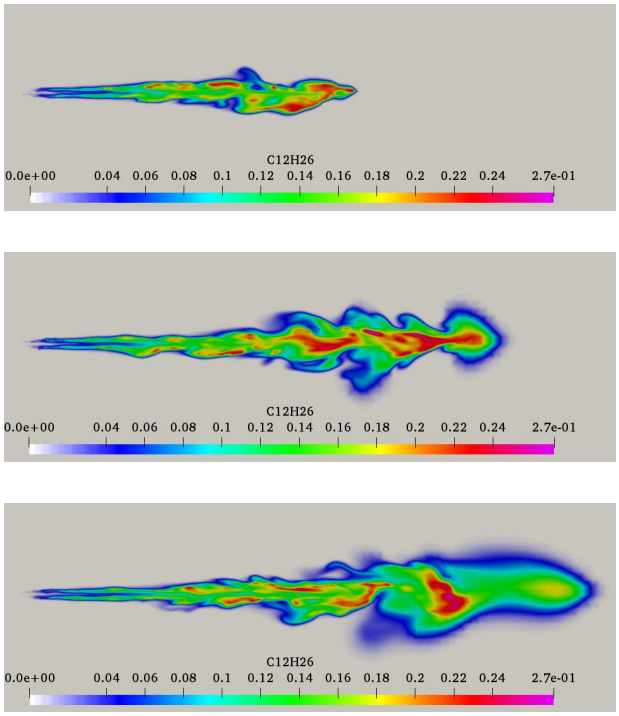

Figure 4: RD break-up model. Fuel vapor mass fraction field near the nozzle at t= 0.08, 0.16 and 0.24 [ms].

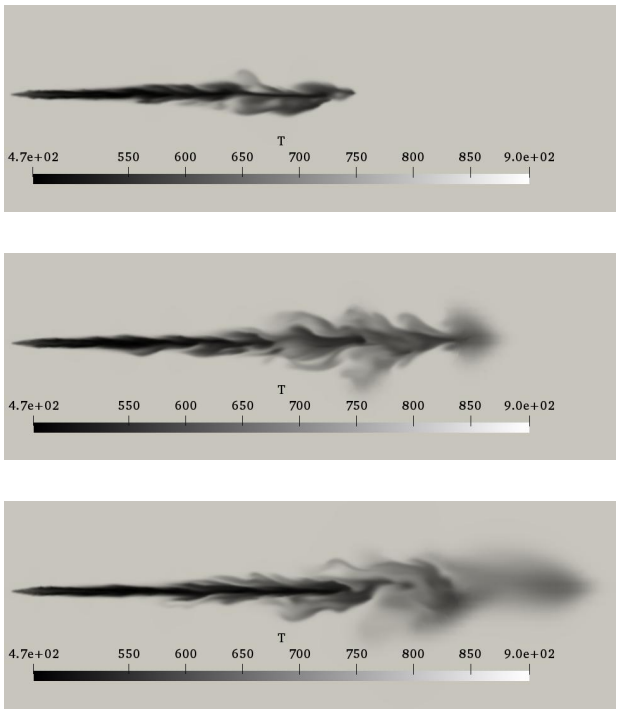

Figure 5: RD break-up model. Temperature field near the nozzle at t= 0.08, 0.16 and 0.24 [ms].

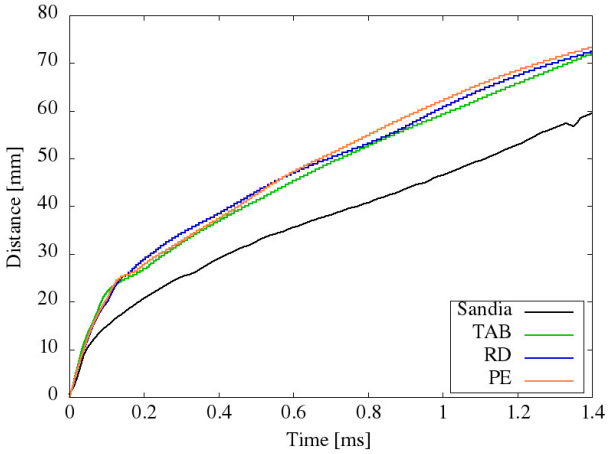

Figure 6: Vapor penetration distance.

three cases, together with the experimental data of Sandia Spray A. Figure 6 shows that the vapor penetration length calculated in all simulations captures perfectly the ramp inclination angle, but over-predicts the vapor penetration length itself.

We remark that even though the models are based on fairly simple physical concepts, their predictions for both liquid and vapor penetration lengths agree quit well with the experimental data. Overall, the deviation between simulation and experimental results can be attributed to initial parcel velocity and to the model constants, which in our study are experimentally tuned.

6. Conclusions

Large Eddy Simulations of liquid fuel injection, break-up, evaporation and eventual mixing with hot ambient gas have been carried out using different break-up models. The initial and boundary conditions for the simulations come from the experiment, Spray A performed at Sandia National Laboratories and made available by the Engine Combustion Network. The validity of three different droplet break-up models (Taylor Analogy Break-up, Reitz-Diwakar and Pilch-Erdman), have been assessed by comparing predictions of global quantities such as liquid penetration and fuel vapor penetration against the experimental results. The results show that the TAB model better captures the liquid penetration, in contrast to RD and PE models that over-predict the liquid penetration. This is due to the fact that the TAB model captures more of the relevant physics for the initial conditions used in this study. The fuel vapor penetration is overpredicted in all three cases, however all models predict the same rate of increment. The three models are based on different physical concepts of droplet disintegration, but none captures all of the relevant modes of break-up. Consequently discrepancies, in terms of break-up initiation time and duration, exist between the simulations and the experimental results, independent of the model used. Our future efforts will focus on the development and implementation of a more physically representative model for droplet break-up.

Acknowledgments

Financial support for the 1st author has been provided by the ERANET BiofCFD program.

References

[1] H. Grosshans, E. Berrocal, E. Kristensson, R. Szász, Int. J. Multiphas. Flow **33** (2015)

[2] A. Favre, Phys. Fluids **26**, 2851 (1983)

[3] X. Chai, K. Mahesh, J. Fluid Mech. **699**, 385 (2012)

[4] A. Yoshizawa, Phys. Fluids **29**, 2152 (1987)

[5] S. Yoon, J. Hewson, P. DesJardin, D. Glaze, A. Black, R. Skaggs, Int. J. Multiphas. Flow **30**, 1369 (2004)

[6] D. Liu, A. B. Mather, R.D. Reitz, SAE Technical Paper Series, 930072 (1993)

[7] H. Grosshans, Large Eddy Simulation of Atomizing Sprays. Ph.D. thesis, Lund University (2013)

[8] H. Grosshans, E. Berrocal, E. Kristensson, R. Szász, L. Fuchs, 12th International Conference on Liquid Atomization and Spray Systems (2012)

[9] A.A. Amsden, P.J. O'Rourke, T.D. Butler, Los Alamos National Lab. REP. LA-11560-MS DE89012805 (1989)

[10] P.J. O'Rourke, A.A. Amsden, SAE Technical Paper Series, 872089 (1987)

[11] R.D. Reitz, R. Diwakar, SAE Technical Paper Series, 870598 (1987)

[12] M. Pilch, C.A. Erdman, Int. J. Multiphas. Flow **13**, 741 (1987)

[13] H. Lamb, *Hydrodynamics*, 6th edn. (Dover, 1945)

[14] J.A. Nicholls, NASA-SP-194 Technical Report pp. 126–128 (1972)

[15] L.P. Hsiang, G.M. Faeth, Int. J. Multiphas. Flow **18**, 635 (1992)

[16] *https://ecn.sandia.gov/*

[17] A. Burcat, B. Ruscic, Argonne National Laboratory Technical Report ANL-05/20 and Technion – Israel Inst. of Tech. Report TAE 960 (2005)

[18] H.G. Weller, G. Tabor, H. Jasak, C. Fureby, Comput. Phys. **12**, 620 (1998)